ACS APPLIED ENERGY MATERIALS

www.acsaem.org Article

Tunable Supercapacitor Materials Derived from Hydrochar/Gold Nanograpes

Daniel Arenas Esteban,* Andrés Guerrero Martínez, Javier Carretero González, Viola I. Birss, Luis C. Otero-Díaz, and David Ávila Brande*

Cite This: *ACS Appl. Energy Mater.* 2020, 3, 9348−9359 Read Online

ACCESS | Metrics & More | Article Recommendations | Supporting Information

ABSTRACT: Since electrode materials play a crucial role in the performance of supercapacitors, the design of architectures based on carbon nanocomposites can enhance the electrochemical performance based on the synergistic effect between the components. Here, we have devised a facile synthetic route for the preparation of a C/Au nanocomposite, denoted as carbon/gold nanograpes (C/Au NGs), based on the hydrothermal polymerization of glucose-stabilized gold nanoparticles. Carbonization/activation of the C/Au NGs at 500 °C yields microporous carbon nanospheres containing several Au nanoparticles, giving a high volumetric capacitance. However, this volumetric capacitance suffers a dramatic drop at fast charge/discharge rates. When heating the C/Au NGs at 700 °C, the Au nanoparticles melt and flow out of the carbon nanospheres, altering the micropore structure of the C/Au NGs shells, and recrystallize at the surface, while some nanoclusters containing only a few Au atoms remained homogeneously dispersed within the pore network of the carbon shell. These nanostructural changes result in an increase in the ionic transport rates across the carbon shell as well as a lowering of the resistance, thus increasing the volumetric capacitance in aqueous acidic solutions and showing a remarkable improvement in the capacitance retention.

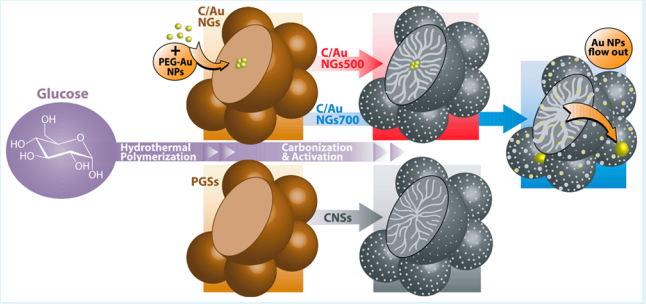

KEYWORDS: *hydrothermal polymerization, carbonaceous gold nanograpes, carbon−gold nanocomposites, supercapacitor, energy storage*

INTRODUCTION

Electrical double-layer capacitors (EDLC), also called supercapacitors, are electrochemical energy storage devices able to deliver a higher amount energy than a dielectric capacitor while also exhibiting higher power densities than batteries.[1] Moreover, supercapacitors can display excellent reversibility, exceptional cyclability (>1 000 000 cycles), and very good electrochemical stability.[2−4] These devices present neat energy solutions in applications where a rapid energy boost is required,[5] such as in the brake energy recovery systems of electric and hybrid vehicles or applications where the lifetime is a more important factor than the energy density, such as in autonomous wireless sensor systems.[6] Nowadays, current research efforts are focused on improving the energy density without losing power density in order to surpass the virtues of rechargeable batteries while maintaining the lifetime properties.[7]

In EDLC, the charge is stored and delivered via the reversible electrostatic attraction/release of electrolyte ions to/from the porous electrodes surface, assembling an electrochemical double layer upon application of an external electric field. In general, during double layer formation, no Faradaic reactions occur at the electrode−electrolyte interface (carbons with quinol/quinone groups on their surface do also exhibit Faradaic reactions) and the energy remains stored as aggregated charges in this region.[8] The electrode material used in an EDLC must exhibit a highly accessible specific surface area as well as be electrochemically stable. Carbon materials are most commonly used for this purpose.[9]

In order to improve performance, a high specific surface area (SSA) and optimized microporous structure are needed so that the electrolyte ions can be rapidly injected/expelled into/out of the carbon pores, even at high current densities. However, control of the SSA and pore size in carbon materials is not straightforward. One approach involves the creation of templated carbons,[10−12] where the pore structure and size can be tuned to be in the mesoporous range. This process involves several stages, which increase the production cost, such as template synthesis, carbon precursors infiltration, carbonization, and elimination of the template.[9] The preparation of carbide-derived carbons (CDC), where the

Received: July 19, 2020
Accepted: August 19, 2020
Published: August 19, 2020

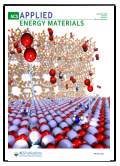

https://dx.doi.org/10.1021/acsaem.0c01711
ACS Appl. Energy Mater. 2020, 3, 9348−9359

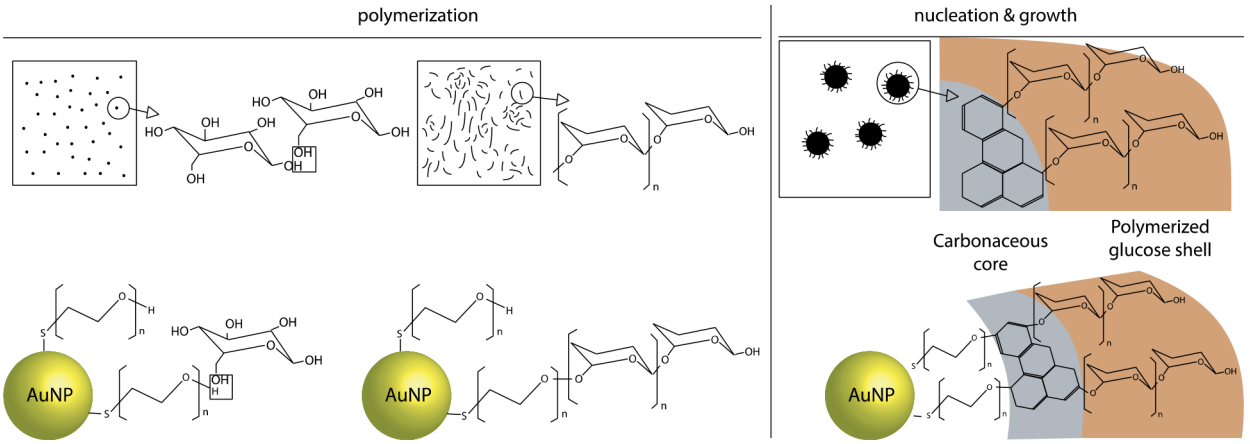

Figure 1. Schematic of nucleation and growth of polymerized glucose spheres (PGS) on carbon cores and mimetic PEG-functionalized Au NP.

micropores network proceed directly from the carbide crystalline structure and additionally can be tuned via temperature treatment,[13] is another strategy to control the pore size of carbon materials, where an increase of the capacitance has been associated with the presence of subnanometer pores.[14,15] Even so, the metal carbide precursor implies a high cost in the CDC's production. Biomass-derived carbons are more convenient in terms of their renewable feedstock, sustainability, lower cost, and environmental friendliness of the precursors, but these types of materials normally present a very heterogeneous and uncontrollable pore structure.[16,17]

The density of the carbon material is another important property related to their applicability as electrodes in supercapacitors. Usually, activated carbons exhibit a relatively low density that limits their volumetric energy density, and therefore these materials are not suitable for practical applications in portable devices, such as sensors, mobile phones, or wearable electronics, among others.[18] For this reason, many efforts have been dedicated to increasing the density of carbons, for example, by the assembly of graphene-based materials, yielding high volumetric performance,[19] or the design of core−shell structures composed of a dense core surrounded by a microporous and high-surface area shell.[20] In these core−shell materials, the combination of several components with complementary properties has been shown to lead to enhanced electrochemical performance. Thus, highly conductive metallic cores can facilitate the transfer of charge in/out of the large surface area microporous carbon shell.

In this work, we have used glucose as the carbon precursor material, as glucose is abundant, cheap, and renewable. This simple sugar can be hydrothermally treated to form polymerized glucose spheres (PGS, also named hydrochar) of different sizes by controlling the temperature and reaction time.[21−25] In a subsequent carbonization step, the nanospheres maintain their original size, but an internal micropore network is formed, albeit with no control over the process. We have also included a very small amount of Au in the synthesis step to further enhance electrochemical performance, similar to approaches that have been reported previously.[26,27] Here, we have developed a green and facile synthetic procedure to incorporate a small amount (up to five ∼15 nm gold nanoparticles (Au NPs) into the core of polymerized glucose spheres (PGS) that are ∼150 nm in diameter, producing a new sustainable hydrochar material, denoted as "C/Au nanograpes" (C/Au NGs), based on their grape-like morphology. This composite material has a relatively low surface area (∼23 m^2 g^{-1}), but carbonization and chemical activation at moderate temperatures result in the production of composite materials with very proficient electrochemical performance. When activated at 500 °C, the C/Au NGs500 materials were obtained, retaining the original nanostructure of the C/Au NGs, while the hydrochar was converted into a carbon-based microporous structure. For comparison, PGS alone, carbonized at the same temperature, also formed carbon nanospheres (CNSs) but without the Au NPs inside. In order to clarify all materials synthesized in this work, a complete scheme can be found in the Supporting Information file (Figure S1).

We show here that the C/Au NGs500 material gives a gravimetric capacitance that is 30% less than for the CNSs containing no Au (119 versus 171 F g^{-1}, respectively). However, the presence of a dense core of Au NPs results in an improvement in the volumetric performance, yielding similar values of ∼90 F cm^{-3} for both materials, which is in the typical range of activated porous carbons (60−100 F cm^{-3}).[28] Unfortunately, the charge/discharge rates of the CNSs and the composite C/Au NGs500 material are roughly the same, quickly decreasing as the charge/discharge rate increases, due to the low electric conductivity of these carbon materials.

To further investigate the structural futures and the evolution of the electrochemical performance of the C/Au NG material carbonized at higher temperatures, it was heated at a carbonization temperature of 700 °C, giving C/Au NGs700. In contrast to C/Au NGs500, this new material did not retain the Au NPs inside the carbon spheres. Instead, the Au NPs were seen to have melted out of the spheres, altering the micropore structure of the C/Au NGs shells and recrystallizing at the surface, while some nanoclusters containing only a few Au atoms remained homogeneously dispersed within the pore network of the carbon shell. These changes resulted in an increase in the ionic transport rates across the carbon shell as well as a lowering of the resistance, thus increasing the volumetric capacitance to ∼115 F cm^{-3} in aqueous acidic solutions and showing a remarkable improvement in the capacitance retention over the range of current densities measured. Notably, these types of Au nanocluster/carbon composites are attracting the interest of many researchers due to their potential use in catalytic and biomedical applications.[29,30]

https://dx.doi.org/10.1021/acsaem.0c01711
ACS Appl. Energy Mater. 2020, 3, 9348−9359

RESULTS AND DISCUSSION

Glucose-derived carbon materials can be easily nanostructured, since glucose is readily hydrothermally converted into solid carbonaceous spheres by polymerization.[31,32] The size of these polymerized glucose spheres (PGS) can be easily tuned by controlling the temperature and reaction time during the hydrothermal synthesis. The PGS synthesis involves a balance between the formation and growth of carbon nuclei. As previously reported, the higher is the temperature, the greater is the number of nuclei formed, with each sphere growing only slowly, yielding a carbonaceous material mainly composed of small spheres. Conversely, the synthesis at low temperature results in the formation of fewer nuclei and favored growth, producing a carbonaceous material consisting of a few large spheres.[21]

In terms of the reaction time, in general, the longer is the reaction time, the larger is the size of the spheres. Glucose polymerization begins with dehydration at the hydroxyl groups, yielding large hydrophilic chains, which subsequently condense into hydrophobic cores that retain a hydrophilic shell that allows for steady growth,[32,33] as shown in Figure 1. Poly(ethylene glycol) methyl ether (PEG-SH) was selected here as the surfactant polymer to enhance the stabilization of face centered cubic Au nanoparticles (Au NPs, see Figure S2) in aqueous solutions, as well as to ensure the polymerization between this polymer and glucose, as PEG has been extensively studied for its molecular aggregation, drug encapsulation, and drug release properties in sugar-PEG-based polymeric architectures.[34] The incorporation of these PEG-functionalized Au NPs during hydrothermal synthesis generates metallic Au cores that are stabilized through linkages to the PEG-SH groups. Glucose can then polymerize at these sites via a dehydration reaction between the OH groups within glucose and at the end of the PEG-SH chains. This is similar to how glucose polymers grow over their own formed cores (Figure 1), favoring the formation of a composite C/Au material. Assuming that the PEG-functionalized Au NPs can mimic the nuclei of the spheres, a very low temperature of 150 °C (in comparison to that of conventional polymerized glucose spheres (PGS) hydrothermal synthesis) over a long reaction time (20 h) was selected in the present work, in order to avoid the formation of new carbon cores. The SEM micrographs displayed in Figure 2 show the synthesized C/Au nanogrape (C/Au NGs) material, showing highly uniform carbonaceous spheres ~150 nm in diameter containing a few (1−5) Au NPs ~15 nm in diameter in the core, similar to the seeds seen inside grapes. For comparison purposes PGS of comparable average size, but without any Au NPs present, were synthesized at a higher temperature but with heating during a shorter reaction time (180 °C for 6 h).

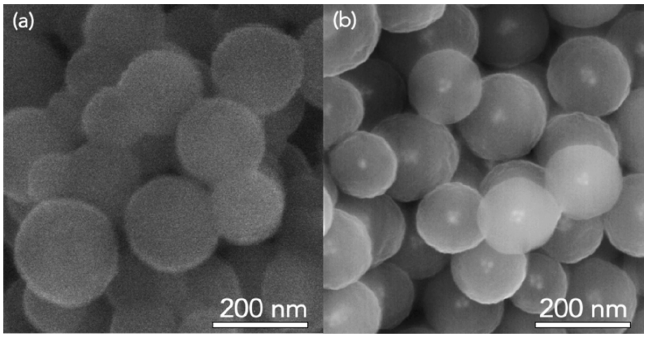

Figure 2. SEM micrograph of (a) polymerized glucose spheres (PGS) and (b) C/Au nanograpes (C/Au NGs) ~150 nm in diameter, where the Au NPs can be clearly observed as small bright spots within, similar to the seeds inside grapes.

The thermal evolution of the C/Au nanograpes with temperature in two different atmospheres, N_2 and air, was evaluated by thermogravimetric analysis (TGA) (Figure S3). Under a flow of N_2, we detect two weight losses, the first from room temperature to 150 °C, attributed to removal of physiosorbed water, and the second between 300 and 1000 °C, indicating a reorganization of the carbon motifs with simultaneous loss of volatile species. It is important to notice that the mass loss at 500 and 700 °C, which are the temperatures selected for carbonization, gives a 64% and 52% residual mass, respectively.

Also, the amount of Au in the C/Au nanograpes was determined by TGA in air to be 2.6 wt %. Considering the large mass of Au vs carbon, this verifies that the amount of Au present in these materials is very small, consistent with the SEM images in Figure 2, thus keeping the cost low as well.

During the polymerization, carbonization, and chemical activation processes required to produce the C/Au nanograpes, infrared spectra provided information on the evolution of surface funtional groups. Polymerized glucose spheres (PGS) and the C/Au nanograpes (C/Au NGs) exhibit analogous spectra but different from that of their glucose precursor (Figure 3a). The major difference lies in the appearance (in the case of the C/Au NGs) of a bands at 1620 cm^{-1}, assigned to C═C vibrations from the aromatic rings, along with a band at 1710 cm^{-1}, assigned to the C═O vibrations corresponding to the carbonyl, quinone, ester, or carboxyl groups that could remain inside the nanospheres. The presence of aromatic groups in the PGS and C/Au nanograpes is supported by the presence of the bands at 875−750 cm^{-1}, assigned to aromatic out-of-plane C−H bending vibrations, and the bands at 3000−2815 cm^{-1}, which correspond to stretching vibrations of the aliphatic C−H groups. Also, the broad band at 3000−3700 cm^{-1}, assigned to the O−H stretching vibration of the hydroxyl or carboxyl groups in both the PGS and the C/Au NGs as well as in the C/Au NG500 composite.[32]

Nevertheless, the intensity of these bands was considerably reduced on carbonized and activated samples, denoting the elimination of these functional groups.[33] If we compare the spectra obtained for the samples carbonized at 500 °C, the CNSs and C/Au NGs500, we notice that the disappearance of the bands in CNSs is most marked, suggesting that the Au NP-containing core prevents the degradation of the hydrochar, likely due to absorption of thermal energy by the metallic nanoparticles; the larger specific heat capacity of gold compared with the polymer implies greater thermal absorption by the nanoparticles, thus reducing the carbonization effect of the polymer in its surroundings. Only when carbonization of the C/Au nanograpes is carried out at 700 °C does the IR spectrum resemble that of the CNSs, although the spectrum still exhibits the bands assigned to the aromatic rings.

Raman spectroscopy was employed to investigate the average structure of the carbon nanospheres (CNSs), as well as the C/Au nanograpes formed at 500 °C (C/Au NGs500) and 700 °C (C/Au NGs700), providing information on the bonding, order and crystallite or domain size. Figure 3b shows the first-order Raman spectra, where the two characteristic bands for disordered carbon materials (the so-called graphite

https://dx.doi.org/10.1021/acsaem.0c01711
ACS Appl. Energy Mater. 2020, 3, 9348−9359

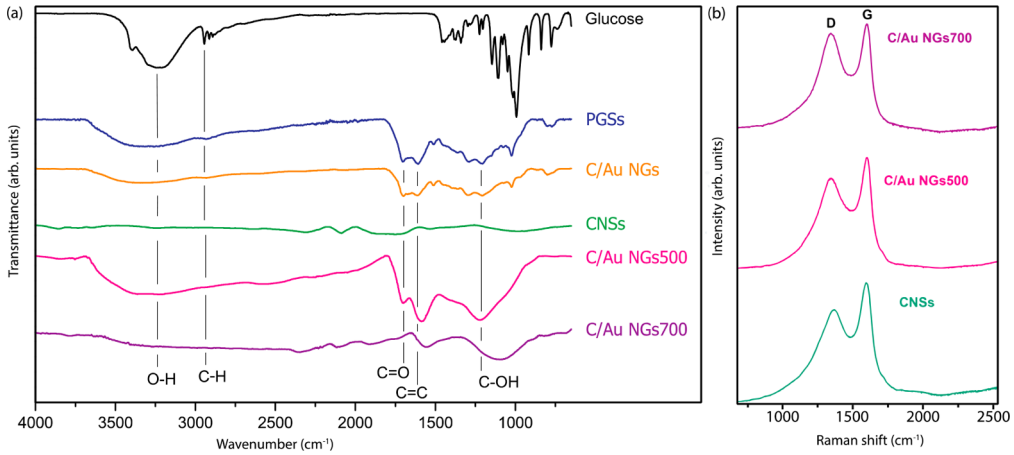

Figure 3. (a) FTIR spectra of glucose, polymerized glucose spheres (PGSs), C/Au nanograpes (C/Au NGs), carbon nanospheres (CNSs), C/Au nanograpes formed by heat-treatment at 500 °C (C/Au NGs500) and C/Au nanograpes formed by heat-treatment at 700 °C (C/Au NGs700). (b) Raman spectra for carbon nanospheres (CNSs), C/Au nanograpes formed at 500 °C (C/Au NGs500), and C/Au nanograpes formed at 700 °C (C/Au NGs700).

(G) band at 1580−1600 cm^{-1} and the disorder−induced (D) band at 1300−1350 cm^{-1}) are identified. In all of our materials, the position, intensity, and FWHM of the G band (Table S1) remain essentially constant, suggesting the same degree of graphitization. On the other hand, the D band is wider than the G one as a consequence of the highly disordered nature of the graphene-like layers that form the carbon shell of these materials. Surprisingly, a slight increase in the D band is noticed when the carbon nanospheres contain Au NPs in their cores, suggesting that their presence favors disorder within the graphene-like layers in the shell. Moreover, the higher intensity of the D band for the C/Au NGs700 material compared to the C/Au NGs500 indicates that this increase in carbonization temperature produces even more disorder in the graphene-like layers. In order to determine the origin of this effect, a TEM study of the local structure of these materials was performed.

The TEM images recorded after the carbonization and activation stages confirm that the carbon nanospheres (CNSs) and the C/Au nanograpes formed at 500 °C (C/Au NGs500) (Figure 4a and Figure 4b, respectively) maintain the spherical shape of their pristine precursors (Figure 2a and Figure 2b). In the case of C/Au NGs500 (Figure 4b), the cores, containing 1−5 Au NPs, are unaffected by the thermal and activation processes. In the case of the C/Au nanograpes formed at 700 °C (C/Au NGs700, Figure 4c), although the spherical shape is preserved, the Au NPs are now mostly on the outer surface of the carbon shell (Figure 4c). Furthermore, these Au NPs within the C/Au NG700 composite are larger than in the C/Au NG material before heating and activation. The TEM image of C/Au NGs700 (Figure 4c) also reveals that the internal core of the carbon spheres is now empty. This indicates that heat-treatment at 700 °C must melt the Au NPs that were originally inside, causing them to pass through the carbon sphere walls and recrystallize as larger Au NPs on the outer surface of the spheres. In addition, it can be noticed that the size of the carbon spheres in the C/Au NG700 composite is slightly smaller than the C/Au NG500 composite. This is likely due to the fact that at higher temperatures, labile functional groups in the hydrochar spheres are eliminated, as confirmed by the IR results (Figure 3b), resulting in a contraction of the spheres.

HAADF-STEM analysis, where the intensity of an image is close to proportional to the atomic number, can offer additional valuable information for these materials, since Au has a higher atomic number than carbon. Figure 4d shows a low magnification HAADF-STEM image of the C/Au NGs700 material, where two spheres with empty cores overlap, suggesting that there is no residual Au remaining within the shell of the carbon spheres. However, a closer inspection at higher magnification (Figure 4e) does show the presence of a few subnanoclusters (just a few Au atoms) in the carbon shell, seen as bright dots that are ∼0.2 nm in size (Figures 4e and S4). This indicates that although most of the melted Au NPs have passed through the carbon shell, nucleating on the other surface, some Au subnanoclusters have recrystallized within the shell structure of C/Au NGs700. Unlike in its bulk form, gold nanoparticles have been reported to be extremely active as a catalyst in several oxidation processes,[35,36] including oxidation of sugars.[37,38] The contact between the gold surface and the reactants is the key to understanding the higher catalytic activity as the particles decrease in size. In this case, melted gold is fully in contact with the pore walls of the carbon host, thus increasing its catalytic activity. In this context, melted gold is capable of oxidizing the CO groups of the hydrochar found along the pore walls, with this being the most probable mechanism of regulating the pore structure and generating these metallic subnanoclusters detected in our HAADF-STEM images.

In order to visualize how the melting of the Au NPs occurs during the 700 °C carbonization of the C/Au NGs, in situ heating TEM analyses were performed (Movie S1). It should be noted that the sample used in this experiment was under high vacuum and without argon flow, and therefore the exact conditions of the carbonization step cannot be exactly reproduced. Even so, Figure 5 shows three TEM images, recorded 0, 15, and 45 min after reaching the final temperature. These images reveal that the Au NPs melt and then flow through the microporous carbon shell framework onto their outer surface where they recrystallize as larger Au NPs. It is noted that the shape and size of the spheres remain unaffected upon heating, consistent with the TEM/HAADF-STEM observations for the C/Au NGs700 material (Figure 4c−e). The transport of Au through the carbon shell at 700 °C,

https://dx.doi.org/10.1021/acsaem.0c01711
ACS Appl. Energy Mater. 2020, 3, 9348−9359

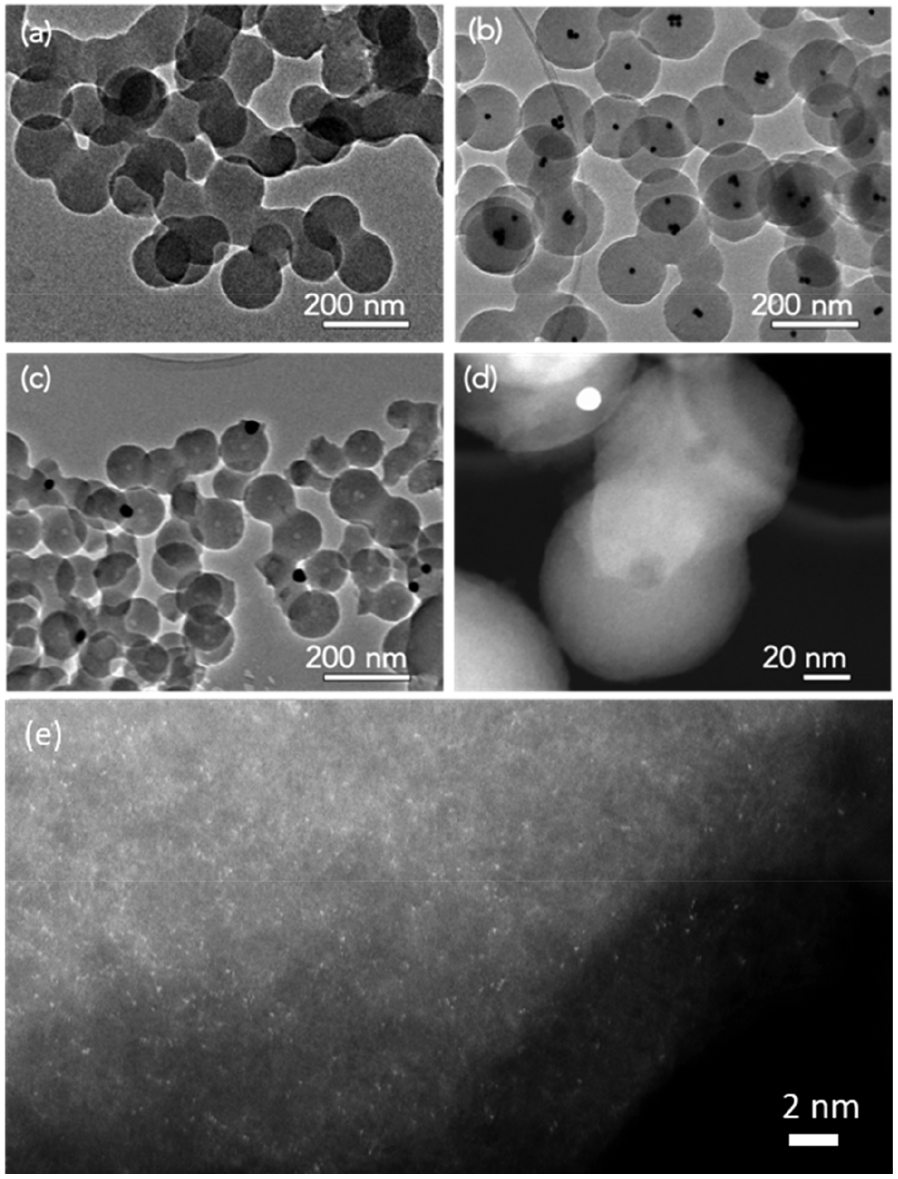

Figure 4. TEM micrographs of (a) carbon nanospheres (CNSs), retaining their original spherical shape with a diameter of ~150 nm, (b) the C/Au NGs500 composite material composed of carbon spheres containing Au NPs within, (c) the C/Au NGs700 composite material composed of hollow carbon spheres with Au NPs now seen on the outer surface of the spheres. (d) HAADF-STEM image of C/Au NGs700, showing the Au NPs located on the outer sphere surfaces, and (e) high resolution HAADF-STEM image collected at the edge of a carbon sphere, where the bright dots indicate the presence of Au nanoclusters (a few Au atoms across).

combined with the high temperature, results in additional disorder as the graphene-like layers rearrange, as was seen from the increased intensity of the Raman D band for the C/Au NGs700 materials (Figure 3b and Table S1).

Since the textural properties are a key factor in producing high performance electrode materials for supercaps, N_2 adsorption−desorption isotherms were measured to extract the specific surface area (S_{BET}) of each sample, as well as the pores size distribution (PSD) (Figure 6), as a function of the thermal treatment. Whereas the as-synthesized C/Au nanograpes (NGs) exhibit poor N_2 uptake across the whole pressure range, the isotherms of carbon nanospheres (CNSs), C/Au NGs500, and C/Au NG700 present a type I shape, which is characteristic of microporous solids.[39] The results obtained for the surface area values, according to BET and nonlocal density functional theory (NLDFT) theories, are collected in Table 1, giving a S_{BET} value as low as 23 m^2 g^{-1} for the C/Au NG hydrochar composite and, as expected, giving higher values for the thermally activated samples. If we compare the surface areas of the two materials prepared under the same synthetic conditions (carbon nanospheres and the C/Au NGs500, both carbonized and activated at 500 °C), the C/Au NG500 material has a smaller surface area, suggesting that the presence of the Au NP cores hinders the development of porosity. However, after carbonization at 700 °C, the surface area of the composite C/Au NG700 slightly surpasses that of the carbon nanospheres (CNSs).

The $S_{2DNLDFT}$ values (Table 1) indicate that the porosity developed in these carbon materials by the heat treatment consists mainly of micropores having a diameter of ~2 nm. This can be explained by considering the structural evolution of the C/Au nanograpes with temperature. On the basis of the

https://dx.doi.org/10.1021/acsaem.0c01711
ACS Appl. Energy Mater. 2020, 3, 9348−9359

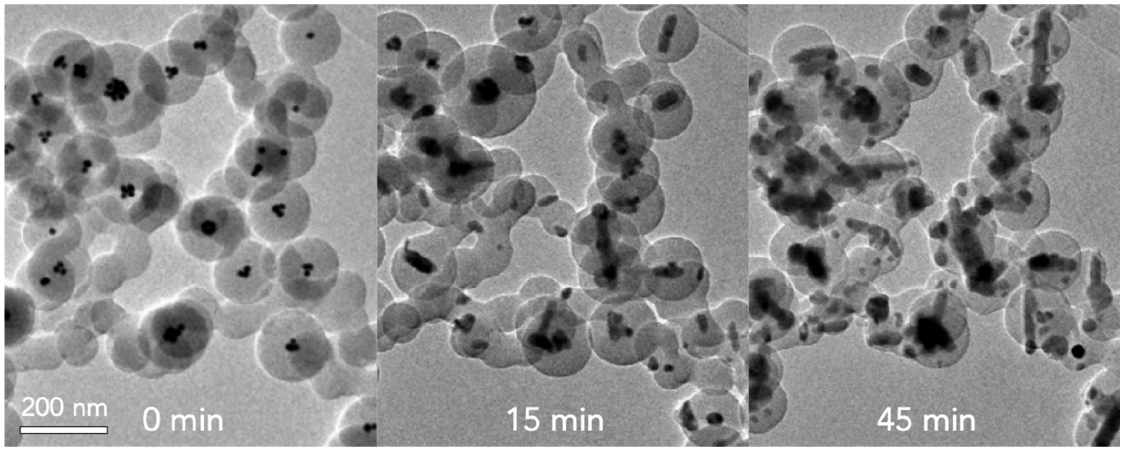

Figure 5. TEM micrographs of the C/Au NGs700 materials with time of in situ heating at 700 °C, where the Au NPs appear to melt and then flow through the walls of the spheres and then recrystallize on the outer surfaces.

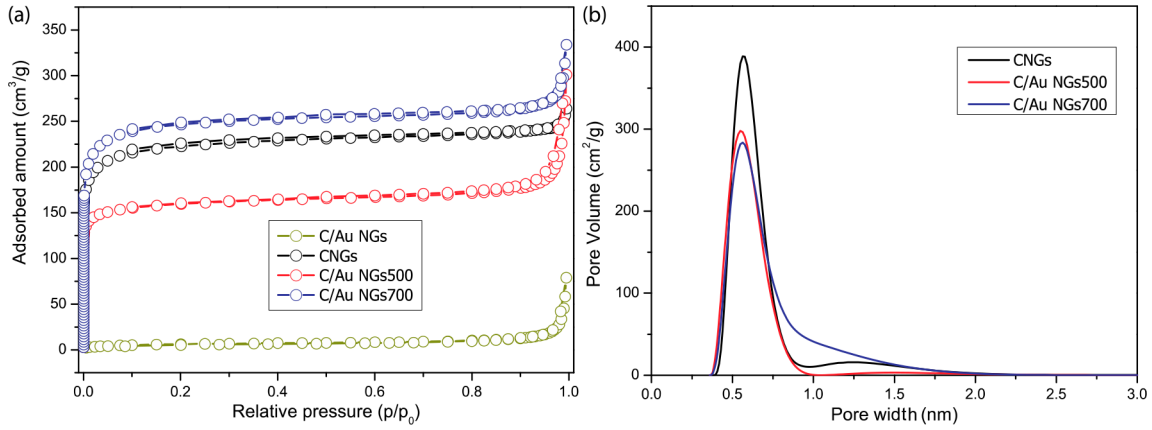

Figure 6. (a) Type I N_2 adsorption isotherms and (b) PSD for the C/Au NGs, carbon nanospheres (CNSs), C/Au NGs500, and C/Au NGs700 materials. The main contribution is centered at 0.56 nm, with minor contributions at 1−2 nm, including a broad tail that unifies both contributions in the case of the C/Au NGs700 composite.

Table 1. Surface Area and Pore Width of the Prepared Samples

sample[a]	S_{BET} (m^2 g^{-1})	$S_{2DNLDFT}$ (m^2 g^{-1})	$S_{2DNLDFT<2nm}$ (m^2 g^{-1})	pore $width_{2D\text{-}NLDFT}$ (nm)
C/Au NGs	23			
CNSs	720	985	976	0.56 and 1.24
C/Au NGs500	515	793	780	0.55
C/Au NGs700	797	1000	992	0.56

[a]C/Au NGs = carbon/gold nanograpes, CNSs = carbon nanospheres, C/Au NGs500 = carbon/gold nanograpes carbonized at 500 °C, C/Au NGs700 = carbon/gold nanograpes carbonized at 700 °C.

Table 2. Capacitance Values Obtained from Three and Two Electrode Experiments and Related Energy and Power Densities

sample	$C_{gravimetric}$ [a] ($F{\cdot}g^{-1}$)	$C_{gravimetric}$ [b] ($F{\cdot}g^{-1}$)	$d_{electrode}$ ($g{\cdot}cm^{-3}$)	$C_{volumetric}$ [b] ($F{\cdot}cm^{-3}$)	E (Wh/kg)	P (W/kg)
CNSs	191	170	0.56	96	5.9	24.8
C/Au NGs500	205	118	0.75	89	4	24.8
C/Au NGs700	436	210	0.54	114	7.2	24.9

[a]Three-electrode configuration. [b]Two electrode configuration.

analysis of the FTIR spectra (Figure 3a), the presence of a thermally conducting core containing several Au NPs in the C/Au NGs prevents the elimination of labile surface functional groups. Therefore, the increase in the surface area progresses more slowly for those materials with Au NPs in their cores than for the PGS without any Au Nps.

The PSD data depicted in Figure 6b reveal that the three materials studied here have a well-defined pore structure with a narrow distribution of micropores with a size centered at 0.56 nm (Table 1). In the case of the carbon nanospheres (CNSs) and the C/Au NGs500 material, the PSD ranges from 1 to 1.5 nm, indicating that the incorporation of the Au NPs does not affect the pore size after carbonization and chemical activation

https://dx.doi.org/10.1021/acsaem.0c01711
ACS Appl. Energy Mater. 2020, 3, 9348−9359

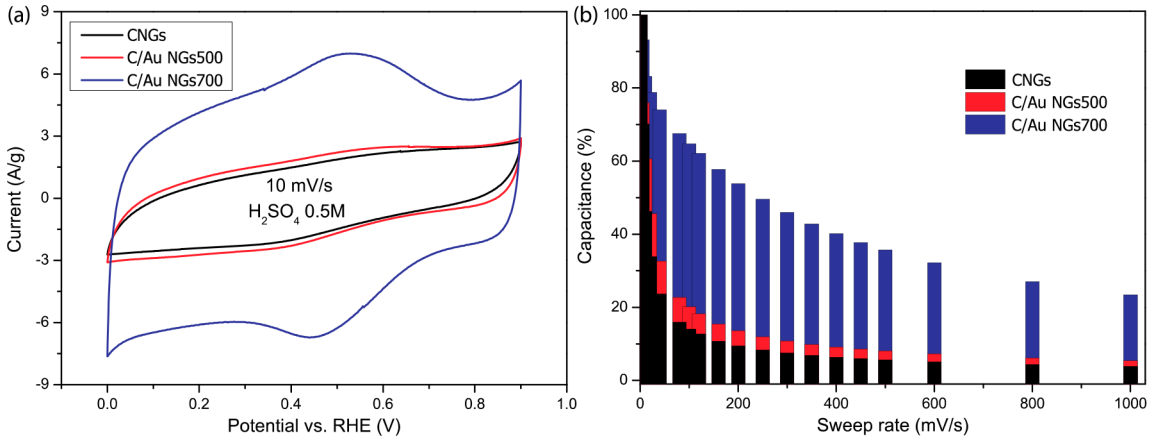

Figure 7. (a) Cyclic voltammograms of carbon nanospheres (CNSs), C/Au NGs500 and C/Au NGs700 at 10 mV s^{-1} using a glassy carbon rod as the working electrode (WE), a reversible hydrogen electrode (RHE) as the reference electrode, and platinized platinum as the counter electrode (CE) in a three-electrode cell configuration. The electrolyte was deaerated 0.5 M H_2SO_4 in deionized water. (b) Capacitance retention of each material with increasing sweep rate.

at 500 °C. However, for the C/Au NGs700 composite, although the main contribution to the PSD is also centered at 0.56 nm, the number of pores with a size ranging between 0.8 and 1.5 nm is higher, generating a wide shoulder that extends to 2 nm. This modification of the PSD is ascribed to the loss of the Au NPs, which also modifies the pore structure of the material and may strongly influence the electrochemical performance.

To determine the capacitive characteristics of these materials (Table 2), cyclic voltammetry (CV) in a three-electrode cell was employed first, as displayed in Figure 7a. A quasi-rectangular shape can be seen in the CV curves belonging to the carbon nanospheres (CNSs) and C/Au NGs500 electrode, typical of carbon materials. High capacitance values of up to 191 F g^{-1} for the CNSs and 205 F g^{-1} for the C/Au NGs500 were obtained at a scan rate of 10 mV s^{-1}. However, the C/Au NGs700 material doubles that values up to 436 F g^{-1} at the same sweep rate (Figure 7a). Additionally, a wide pronounced redox peak centered at ~0.5 V which can be assigned to the pseudocapacitive redox activity can be observed, probably due to the oxygen functional groups attached on the accessible surface of the material.[40] Since polymerized glucose is the precursor material for the CNSs and NG composites, it is not surprising to detect the presence of oxygenated groups on their surfaces. In the case of the C/Au NG700 composite, the new nanopores produced in the walls of the carbon spheres when the Au NPs melt may be quite susceptible to surface functionalization with oxygen groups. The absence of any Au CV features confirms that the total Au surface area is very small, consistent with the ultrasmall loading of Au in these composites.

Although the S_{BET} values of CNSs and C/Au NGs700 are similar (Table 1), the C/Au NGs700 composite gives a much higher electrochemically active surface area (ECSA) than seen for either CNSs or C/Au NGs500. This may indicate that the additional nanopores generated in the carbon shell after Au migration through the shell at 700 °C facilitate the access of the acidic solution to the inside of the spheres, thus allowing charging/discharging of both the inner and outer carbon shell surfaces. Consistent with this, Figure 6b clearly showed a broad shoulder at pore sizes from 0.5 to 1.5 nm in the case of C/Au NGs700, indicating that the outward migration of the Au NPs induces some rearrangement of the porous structure in this range, contrary to the situation for the CNSs and C/Au NGs500.

Importantly, the C/Au NGs700 material was found to lose 47% of its capacitance at 200 mV s^{-1} (Figure 7b), while the carbon nanospheres (CNSs) and C/Au NGs500 lost approximately 70% of their capacitance already at 50 mV s^{-1}. The pore structure generated in the C/Au NGs700 material allows faster ion diffusion, consistent with the larger CV currents seen in Figure 7a. Although the PSD of all of the materials is centered at 0.56 nm (Table 1), the development of a certain number of 0.8−1.5 nm size pores in C/Au NGs700 could be facilitating ion diffusion through these new pathways in the porous framework, especially at fast charge and discharge rates.

In order to evaluate if the synergistic effect between the pore structure and Au subnanoclusters is responsible for the superior electrochemical performance of C/Au NGs700, additional CV experiments have been performed in CNSs carbonized at 700 °C instead 500 °C. As it can be observed in Figure S5, the voltammogram of CNSs carbonized at 700 °C exhibits a similar behavior as CNSs and C/Au NGs500 materials, whereas due to the unique pore structure of the C/Au NGs700 composite arising from the gold leaching process during the synthesis and the presence of some nanoclusters containing Au atoms that remained homogeneously dispersed within the pore network of the carbon shell, this material exhibits the best electrochemical performance. These results support the fact that the melting of the Au NPs is critical in producing the porosity of the C/Au NGs700 composite and to the synergistic effect of pore structure and Au subnanoclusters in the improvement of the gravimetric and volumetric capacitances.

The high gravimetric capacitance obtained from the three-electrode experiments (Figure 7) prompted us to process the materials as micrometer thick electrodes and perform a second electrochemical characterization in a symmetrical configuration with two electrodes. Thus, volumetric capacitance could be extracted from galvanostatic measurements (Table 2), giving a more reliable capacitance value in terms of applicability.[41] A higher current response for the C/Au NGs700 composite material in comparison with the carbon nanospheres (CNSs) and C/Au NGs500 electrode materials was evidenced from the CVs (Figure 8a), following the same trend observed in the

https://dx.doi.org/10.1021/acsaem.0c01711
ACS Appl. Energy Mater. 2020, 3, 9348−9359

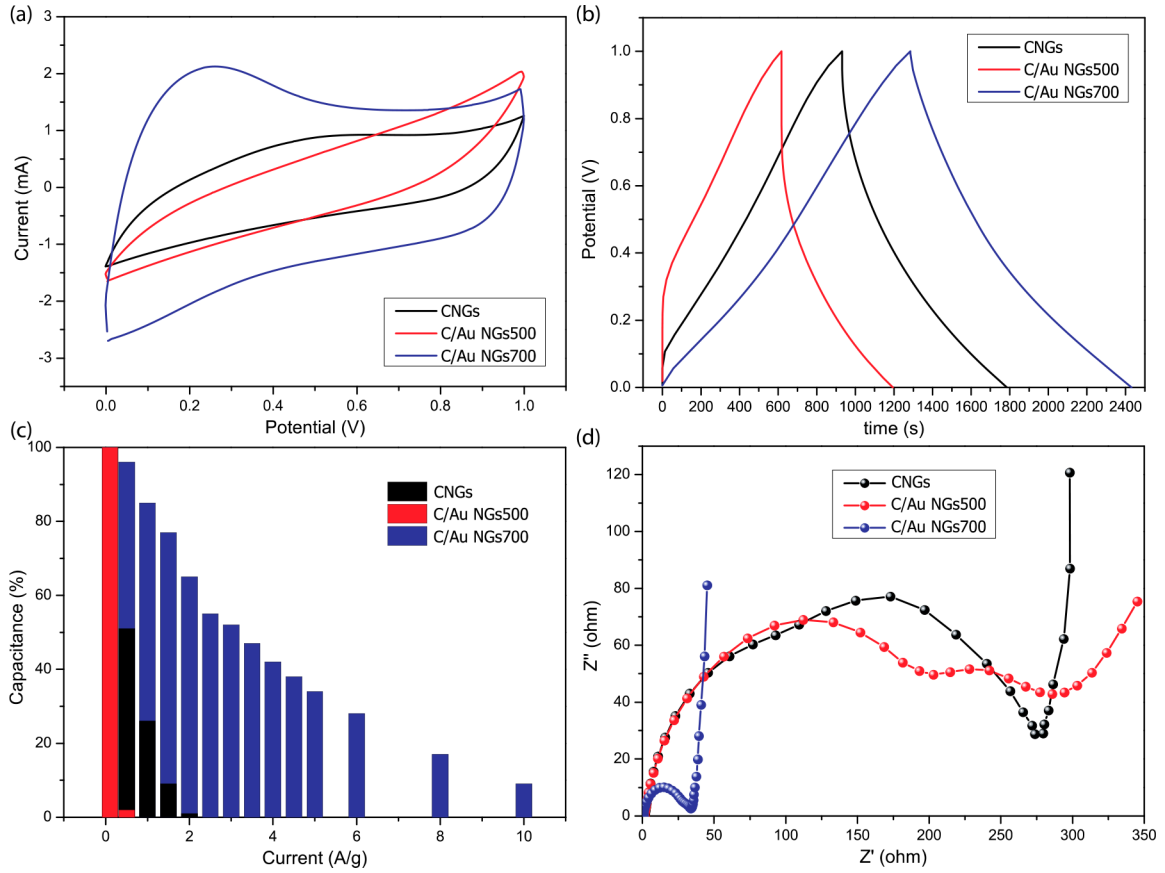

Figure 8. (a) Two-electrode cyclic voltammograms at 5 mV s^{-1} in a Swagelok-type cell, (b) fifth galvanostatic charge−discharge cycle at 0.1 mA g^{-1}, (c) capacitance retention, and (d) Nyquist plots obtained for the carbon nanospheres (CNS), C/Au NGs500 and C/Au NGs700 materials, all in 0.5 M H_2SO_4.

three-electrode experiments (Figure 7). The C/Au NGs700 composite exhibited a distortion of the CV from the ideal rectangular capacitive behavior, likely due to an ion sieving effect produced by the smallest pores on the electrolyte ions.[42] It is also notable that the carbon nanospheres (CNSs) and C/Au NGs500 materials showed a more tilted CV, suggesting that electron and/or ion transport was inhibited in these materials, resulting in a larger *IR* drop. This also indicates that the Au NPs in the core of the microporous carbon spheres of the C/Au NGs500 material are not significantly altering the electrochemical properties of the CNSs. Rather, it is only after Au transport from the inner core to the outer shell surface with heat treatment, producing the larger pores and subclusters of Au within the carbon shell, that benefits are observed in the capacitive characteristics of these materials.[33,43]

The galvanostatic charge−discharge data (Figure 8b) show that the highest gravimetric and volumetric capacitance is achieved by the C/Au NGs700 composite (210 F g^{-1} and 114 F cm^{-3}), in comparison with those of the CNSs (170 F g^{-1} and 96 F cm^{-3}) and C/Au NGs500 materials (118 F g^{-1} and 89 F cm^{-3}) at 0.1 A g^{-1}. These values for C/Au NGs700 are higher than those obtained for carbon spheres in aqueous electrolytes,[44,45] showing the promise of C/Au NGs700 for supercapacitor applications. In addition, the lower ohmic drop seen for C/Au NGs700 vs the carbon nanospheres (CNSs) and C/Au NGs500 materials suggests that C/Au NGs700 has a higher electronic conductivity. In order to investigate this superior performance of C/Au NGs700 at higher charge rates, the Coulombic efficiency for each material was calculated by comparing the charge and discharge times in each galvanostatic cycle at increasing currents (Figure S6). For the CNSs and C/Au NGs500 materials, we observe an irregular variation of the Coulombic efficiency as the current starts to increase and a dramatic drop of the specific capacitance from 1 A·g^{-1}, whereas the C/Au NGs700 composite retains high Coulombic efficiencies up to 95−99% in all cycles but shows a decrease in the specific capacitance with increasing current. These results indicate that the C/Au NGs700 composite electrodes have long-term stability when used in supercapacitor applications.

Since the 500 and 700 °C treated materials exhibit a similar degree of graphitization, based on the Raman spectra (Figure 3b), the higher electrical conductivity of the C/Au NGs700 composite is ascribed to the presence of the Au subnanoclusters within the carbon shell. Also, the larger Au NPs now present on the outer surfaces of the spheres may also improve the intersphere contact, thus lowering the electrical resistance between carbon spheres (Figure 4c and Figure 4e).

Figure 8c shows the capacitance retention of each electrode material during galvanostatic charge−discharge measurements. At higher rates, the carbon nanospheres (CNSs) and C/Au NGs500 materials quickly lose their capacitance at 2.5 and 1 A g^{-1}, respectively, while the C/Au NGs700 composite still retains 50% of its capacitance at ∼3.75 A g^{-1}.

The calculation of the equivalent series resistance (ESR) values for each material was performed from the impedance spectra (Figure 8d). While the carbon nanospheres (CNSs) and C/Au NGs500 materials present analogous charge transfer

https://dx.doi.org/10.1021/acsaem.0c01711
ACS Appl. Energy Mater. 2020, 3, 9348−9359

resistance with at least two large semicircles and ESR values of 140 and 223 Ω cm^2 obtained, respectively, the C/Au NGs700 composite exhibits a lower ESR value of only 32 ohm cm^2. It should be noted that the vertical response at low frequencies is characteristic for the response of a good capacitor, typical of carbon materials,[46] while semicircles reflect a double layer charging process in parallel with a redox process, similar to battery type devices. The larger semicircles seen for the carbon nanospheres (CNSs) and C/Au NGs500 materials indicate the presence of a range of interfaces as well as slow ion diffusion, in contrast to the smaller semicircle for the C/Au NGs700 composite. In addition, the H^+ and SO_4^{2-} diffusion coefficients were calculated for both materials from the impedance data,[47] showing a clear advantage of 1 order of magnitude of the C/Au NGs700 composite relative to the others (Table S2). These results indicate higher ion diffusion rates in the C/Au NGs700 material, suggested to be due to the synergistic effect of the new pore structure developed after the melting of the Au Nps and the presence of well dispersed Au subnanoclusters within the material. This is an important advantage for the use of these materials as electrodes in supercapacitors.

Tailored hydrothermally carbonized sugars have been studied before for use as electrode materials in supercapacitors in aqueous solutions, reaching comparable capacitances as obtained for C/Au NGs700 (Table S3), but in most cases, the rate capabilities need to be increased, achieved by using a dopant, such as carbon black, in the electrochemical measurements. The C/Au NGs700 material overcomes the electrical conductivity problem without any added dopants, due to the gold nanoclusters dispersed within and on the outer surface of the carbon spheres, as well as by the generation of pores in the walls of the spheres. Thus, a novel and efficient methodology has been developed to tailor the pore structure within these carbon-derived composite materials during their synthesis, thus opening up a new direction for the design of nanostructured carbon materials.

CONCLUSIONS

We report here a facile and reproducible method for the synthesis of a novel nanocomposite, involving the controlled hydrothermal preparation of polymerized glucose spheres (PGS) over previously synthesized gold nanoparticles (Au NPs). These are denoted as carbon nanograpes (NGs), based on their shape and the presence of the Au NPs inside the spheres, similar to seeds inside a grape. By carbonization and activation of these nanograpes at 500 °C (C/Au NG500), the original nanogrape-type structure is retained. This produces a denser microporous carbon composite that is able to afford comparable gravimetric capacitances up to 205 F g^{-1} at 5 mV s^{-1} to what is obtained from carbon nanospheres (CNSs) without Au NPs in the core.

However, when the C/Au nanograpes were carbonized at 700 °C, the resulting material (C/Au NG700) gave a capacitance as high as 435 F g^{-1}. At these temperatures, the Au NPs start to melt and flow out of the core, leaving homogeneously dispersed Au subnanoclusters within the pore walls and larger Au NPs on the outer shell surface, enhancing the electrical conductivity of these hydrochar-derived carbon materials. During this process, new nanochannels are produced in the C/Au NG700 shells that enhance ion transport, as supported by the electrochemical results. The C/Au NG700 sample exhibited very high gravimetric and volumetric capacitance values in a symmetrical two-electrode cell of 210 F g^{-1} and 114 F cm^{-3}, respectively.

The present results are of great significance, as they demonstrate a new method of fabricating highly adaptable nanopores in carbon−metal composites, resulting in very promising properties for electrochemical energy storage applications. Furthermore, a new procedure to obtain well dispersed Au subnanoclusters, supported on microporous carbon, has also been developed. This is of great interest due to their potential use in many catalytic and biomedical applications.

METHODS

Chemicals. All the reagents were acquired from commercial suppliers and used without further purification: hydrogen tetrachloroaurate trihydrate ($HAuCl_4 \cdot 3H_2O$, ≥99.9%), sodium citrate dihydrate (>99.9%, Sigma-Aldrich), methyl ether thiol (PEG Thiol-6000, Sigma-Aldrich), and D-(+)-glucose (>99.5%, Sigma-Aldrich) were purchased from Aldrich, and KOH (>84% pellets, EMPLURA) was from EMPLURA. Milli-Q grade water (resistivity 18.2 MΩ cm at 25 °C) was used in all synthesis.

Synthesis of Gold Nanoparticles. Gold nanoparticles (Au NPs) were synthesized following the classical method reported by Enustuna and Turkevich.[48] A solution containing 0.4 mM $HAuCl_4$ dissolved in 500 mL of water was heated at 100 °C in a 1 L round-bottom flask. Then, a second aqueous solution of 20 mL of 1 wt % sodium citrate was directly added under vigorous stirring. The mixture is left to boil for up to approximately 10 min, when the color begins to turn reddish. Once the mixture reached room temperature (RT), the suspension was centrifuged several times at 6500 rpm over 90 min in order to remove the excess reactants, redispersing and concentrating the precipitate in milli-Q water. When the concentration of nanoparticles was higher than 10 mM, poly(ethylene glycol) methyl ether thiol (PEG Thiol-6000) was added to the suspension in a ratio of 4 molecules per 1 nm^2 nanoparticle total surface under stirring overnight for surfactant exchange. The AuNPs were additionally centrifuged again at 1200 rpm over 90 min to clear away possible surfactant excess.

Carbon/Gold Nanograpes (C/Au NGs) and Polymeric Glucose Sphere (PGS) Preparation. The C/Au NGs were prepared by hydrothermal synthesis, where 1.8 g (10 mmol) of D-(+)-glucose was dissolved in 10 mL of a colloidal 0.5 mM suspension of the Au NPs. The mixture was heated up to 150 °C in a stainless-steel autoclave for 20 h. After washing the resulting product with water followed by centrifugation, it was left to dry in a desiccator. Polymeric glucose spheres (PGS) were additionally synthesized following a similar method except that no AuNPs were added to the mixture and the heating conditions were different (180 °C for 6 h).

The synthesized C/Au NGs and PGS materials were deposited in a quartz crucible and heated at 500 °C (PGS and C/Au NGs) or 700 °C (only done for the C/Au NGs) for 1 h inside a tubular furnace under an Ar atmosphere. When the carbonization process ended, the system was cooled to RT and the products were chemically activated with solid KOH. The weight ratio of PGS or the C/Au-NGs to KOH was 1:4. Both materials were ground together in a mortar to achieve a homogeneous mixture. The solid mixture was then located inside the same tubular furnace over an alumina crucible for the next chemical activation process under a continuous flow of Ar for 60 min at 500 °C. The heat was turned off and the system was allowed to cool to 25 °C. The activated products were then washed with water and dried in a desiccator at 110 °C overnight. The samples prepared using these synthetic pathways are denoted as C/Au NGs500 (C/Au NGs carbonized at 500 °C) and C/Au NGs700 (C/Au NGs carbonized at 700 °C), based on the grape-like morphology of these two materials, while the product obtained from just the PGS is denoted as "carbon nanospheres" (CNSs).

https://dx.doi.org/10.1021/acsaem.0c01711
ACS Appl. Energy Mater. 2020, 3, 9348−9359

Characterization. *Scanning Electron Microscopy (SEM).* SEM images were obtained on a JSM 6335 F electron microscope operating at 15 kV at a working distance of 15 mm.

Transmission Electron Microscopy (TEM). Low magnification TEM and high-angle annular dark field scanning-TEM (HAADF-STEM) studies were performed with a JEOL 3000 F (acceleration voltage of 300 kV) microscope (point resolution of 1.7 Å) and in a probe aberration corrected microscope JEOL ARM 200 cF operated at 200 kV.

In situ TEM analyses were performed with a JEOL 2100 (acceleration voltage of 200 kV) microscope (point resolution of 2.5 Å) using a GATAN double tilt heating holder model 652 and a molybdenum grid coated with a holey carbon film instead of the usual copper gridones, in order to prevent grid melting. The C/Au NG material was deposited on the molybdenum grid, which was heated at 5 °C/min to 700 °C, at which melting was clearly observed. This temperature was maintained for 1 h, after which it was gradually reduced to room temperature.

Thermogravimetric Analysis (TGA). TGA was performed using a TA Instruments apparatus (SDT Q600 model) in either a N_2 or O_2 atmosphere. The samples were heated at 5 °C min^{-1} to 600 °C under O_2 or to 1000 °C under N_2.

Infrared spectra were recorded on a PerkinElmer 100 FT-IR spectrometer in the 4000−650 cm^{-1} region. The Raman spectra of the samples were acquired with a confocal dispersive micro-Raman spectrometer NT-MDT NTegra Spectra, using a Spectra-Physics solid state laser operating at 532.0 nm.

Textural characterization was performed by means of N_2 adsorption studies at 77 K using a surface area and porosity analyzer ASAP2020 (Micromeritics). The specific surface area (S_{BET}) was calculated according to BET theory. The SAEIUS software for the 2D nonlocal density functional theory (2D-NLDFT) was used for calculating the pore size distribution (PSDs) by considering the pore walls of the standard carbon slit-shaped pore geometry to be energetically heterogeneous.[49]

Electrochemical Characterization. The materials were first characterized in a three-electrode cell, containing a deaerated 0.5 M H_2SO_4 (95.0−98.0% Sigma-Aldrich) solution as electrolyte, a platinized Pt mesh as the counter electrode (CE), a reversible hydrogen electrode (RHE) as the reference electrode, and a glassy carbon (GC) rod (⌀ = 0.7 cm) as the working electrode (WE), following a procedure previously reported.[50] The carbon-based materials in powder form (0.01 g) were dispersed in 0.4 g of a 1 wt % Nafion/ethanol solution. The suspension was sonicated for 30 min to obtain a carbon/Nafion ink. To form the carbon film, a drop of the ink (11 μL) was deposited on the surface of the WE and dried at room temperature. The specific capacitance (C_{grav} = F g^{-1}) of the carbon film was calculated from the cyclic voltammetry data, using the following equation:

$$C_{grav} = \frac{I}{m_e \Delta \nu} \tag{1}$$

where I is the current response (A) by applying different potentials, m_e is the mass (g) of the active material in a single electrode, and $\Delta\nu$ is the sweep rate (V s^{-1}).

The volumetric capacitance (F cm^{-3}) of the thin film electrodes was determined using a two-electrode Swagelok-type cell, for which a disk-shaped electrode was prepared. The electrodes were prepared by mixing 95 wt % of the carbon material with 5 wt % of polytetrafluoroethylene solution (PTFE 60 wt %, Sigma-Aldrich) as polymer binder. The mixture was mixed by manual stirring using few milliliters of ethanol until a viscous slurry was obtained. The slurry was laminated uniformly with the help of a glass test tube until the final thickness was in the 250−200 μm range. Then the film was dried and kept at 120 °C under vacuum for 12 h prior to each measurement. Electrodes of comparable mass (up to 3 mg and a density of 0.56 g cm^{-3}, 0.75 g cm^{-3}, and 0.54 g cm^3 for the CNSs, C/Au NGs500, and C/Au NGs700 electrodes, respectively) and 10 mm in diameter were assembled in the symmetrical Swagelok-type cell, wetted with the electrolyte, separated with a glass fiber membrane (Whatman glass microfiber filters, grade GF/B, 12.7 mm in diameter), and placed in direct contact with the Ti current collector.

Electrochemical studies were performed in aqueous 0.5 M sulfuric acid (95.0−98.0% Sigma-Aldrich) over a voltage window ranging from 0 to 1 V vs the RHE. Cyclic voltammetry (CV) at 5 mV s^{-1}, as well as galvanostatic measurements at current densities ranging from 0.1 to 10 A g^{-1}, was performed under ambient conditions using a multichannel potentiostat/galvanostat (Biologic VMP3). Coulombic efficiency was calculated from galvanostatic curves according to the following equation:

$$C_{ef} = \frac{t_D}{t_C} \times 100 \tag{2}$$

where t_C and t_D are the charge and discharge times, respectively. Electrochemical impedance spectroscopy (EIS) measurements were also performed by applying a low sinusoidal amplitude voltage of 10 mV to the working electrode at frequencies ranging from 1 MHz to 10 mHz using the above-mentioned multichannel potentiostat/galvanostat, all at the OCP. The specific capacitance (C_{grav}) of the working electrode was calculated from the galvanostatic charge−discharge plot using the following equation:

$$C_{grav} = \frac{2It}{m_e \Delta E_{cell}} \tag{3}$$

where I is the current (A), m_e refers to the mass (g) of active material in a single electrode, t is the time (s) needed to complete the charge or discharge at up to 1 V vs OCV in the symmetric configuration, and ΔE_{cell} is the potential (V) between the WE and RE. The volumetric capacitance was obtained by multiplying the gravimetric capacitance by the density of the electrode film.

■ ASSOCIATED CONTENT

Supporting Information

The Supporting Information is available free of charge at https://pubs.acs.org/doi/10.1021/acsaem.0c01711.

Scheme of synthesized materials, HRTEM image of AuNPs, thermogravimetric analysis, HR-STEM images of C/Au NGs700, parameters derived from Raman spectra, three-electrodes cyclic voltammetry, capacitance and Coulombic efficiency, ion diffusion coefficient, and performance of reported carbon-based supercapacitors on aqueous electrolytes (PDF)

Movie S1 of in situ TEM experiment (MP4)

■ AUTHOR INFORMATION

Corresponding Authors

Daniel Arenas Esteban − *Departamento de Química Inorgánica, Universidad Complutense de Madrid, 28040 Madrid, Spain*; Email: darenas@ucm.es

David Ávila Brande − *Departamento de Química Inorgánica, Universidad Complutense de Madrid, 28040 Madrid, Spain*; orcid.org/0000-0003-0452-2482; Email: davilabr@ucm.es

Authors

Andrés Guerrero Martínez − *Departamento de Química Física, Universidad Complutense de Madrid, 28040 Madrid, Spain*; orcid.org/0000-0001-8576-2896

Javier Carretero González − *Institute of Polymer Science and Technology, ICTP-CSIC, 28006 Madrid, Spain*; orcid.org/0000-0002-8008-5715

Viola I. Birss − *Department of Chemistry, University of Calgary, Calgary, AB T2N 1N4, Canada*

Luis C. Otero-Díaz − *Departamento de Química Inorgánica, Universidad Complutense de Madrid, 28040 Madrid, Spain*

https://dx.doi.org/10.1021/acsaem.0c01711
ACS Appl. Energy Mater. 2020, 3, 9348−9359

Complete contact information is available at:
https://pubs.acs.org/10.1021/acsaem.0c01711

Author Contributions

The manuscript was written through contributions of all authors. All authors have given approval to the final version of the manuscript.

Notes

The authors declare no competing financial interest.

■ ACKNOWLEDGMENTS

We thank the Spanish Ministry of Economy, Industry and Competitiveness (MINECO) through a Ramon y Cajal Fellowship (Grant RYC-2015-17722) and funding from the Retos Projects (Grants MAT2017-84385-R and MAT2017-86796-R, AEI/FEDER/UE), as well as the Natural Sciences and Engineering Research Council of Canada (NSERC) for the overall support of this work.

■ ABBREVIATIONS

EDLC = electrical double-layer capacitor
SSA = specific surface area
CDC = carbide-derived carbons
PGS = polymerized glucose spheres
Au NPs = gold nanoparticles
C/Au NGs = carbon/gold nanograpes
C/Au NGs500 = carbon/gold nanograpes carbonized at 500 °C
C/Au NGs700 = carbon/gold nanograpes carbonized at 700 °C
CNS = carbon nanosphere

■ REFERENCES

(1) Conway, B. E. *Electrochemical Supercapacitors: Scientific Fundamentals and Technological Applications*; Kluwer Academic/Plenum Publishers: New York, 1999.
(2) Simon, P.; Gogotsi, Y. Materials for electrochemical capacitors. *Nat. Mater.* **2008**, *7*, 845−854.
(3) Pan, S.; Lin, H.; Deng, J.; Chen, P.; Chen, X.; Yang, Z.; Peng, H. Novel Wearable Energy Devices Based on Aligned Carbon Nanotube Fiber Textiles. *Adv. Energy Mater.* **2015**, *5*, 1401438.
(4) Chin, K. C.; Green, N. W.; Brandon, E. J. Evaluation of supercapacitors for space applications under thermal vacuum conditions. *J. Power Sources* **2018**, *379*, 155−159.
(5) Ceraolo, M.; Lutzemberger, G.; Meli, E.; Pugi, L.; Rindi, A.; Pancari, G. Energy storage systems to exploit regenerative braking in DC railway systems: Different approaches to improve efficiency of modern high-speed trains. *Journal of Energy Storage* **2018**, *16*, 269−279.
(6) Staaf, L. G. H.; Lundgren, P.; Enoksson, P. Present and future supercapacitor carbon electrode materials for improved energy storage used in intelligent wireless sensor systems. *Nano Energy* **2014**, *9*, 128−141.
(7) Zhang, L.; Hu, X.; Wang, Z.; Sun, F.; Dorrell, D. G. A review of supercapacitor modeling, estimation, and applications: A control/management perspective. *Renewable Sustainable Energy Rev.* **2018**, *81*, 1868−1878.
(8) Lu, P.; Xue, D.; Yang, H.; Liu, Y. Supercapacitor and nanoscale research towards electrochemical energy storage International. *Int. J. Smart Nano Mater.* **2013**, *4*, 2−26.
(9) Zhang, L. L.; Zhao, X. S. Carbon-based materials as supercapacitor electrodes. *Chem. Soc. Rev.* **2009**, *38*, 2520−2531.
(10) Wang, Y. S.; Wang, C. Y. Templated mesoporous carbons and their performance for electric double layer capacitors. *New Carbon Materials* **2010**, *25*, 376−381.
(11) Sevilla, M.; Álvarez, S.; Centeno, T. A.; Fuertes, A. B.; Stoeckli, F. Performance of templated mesoporous carbons in supercapacitors. *Electrochim. Acta* **2007**, *52*, 3207−3215.
(12) Tang, D.; Hu, S.; Dai, F.; Yi, R.; Gordin, M. L.; Chen, S.; Song, J.; Wang, D. Self-Templated Synthesis of Mesoporous Carbon from Carbon Tetrachloride Precursor for Supercapacitor Electrodes. *ACS Appl. Mater. Interfaces* **2016**, *8*, 6779−6783.
(13) Gogotsi, Y.; Nikitin, A.; Ye, H.; Zhou, W.; Fischer, J. E.; Yi, B.; Foley, H. C.; Barsoum, M. W. Nanoporous Carbide Derived Carbon with Tunable Pore Size. *Nat. Mater.* **2003**, *2*, 591−594.
(14) Chmiola, J.; Dash, R.; Yushin, G.; Gogotsi, Y. Effect of pore size and surface area of carbide derived carbons on specific capacitance. *J. Power Sources* **2006**, *158*, 765−772.
(15) Jänes, A.; Lust, E. Electrochemical characteristics of nanoporous carbide-derived carbon materials in various non-aqueous electrolyte solutions. *J. Electrochem. Soc.* **2006**, *153*, A113−A116.
(16) Jung, S. H.; Myung, Y.; Kim, B. N.; Kim, I. G.; You, I. K.; Kim, T. Y. Activated Biomass-derived Graphene-based Carbons for Supercapacitors with High Energy and Power Density. *Sci. Rep.* **2018**, *8*, 1915.
(17) Hu, B.; Wang, K.; Wu, L.; Yu, S. H.; Antonietti, M.; Titirici, M. M. Engineering Carbon Materials from the Hydrothermal Carbonization Process of Biomass. *Adv. Mater.* **2010**, *22*, 813−828.
(18) Li, P.; Li, H.; Han, D.; Shang, T.; Deng, Y.; Tao, Y.; Lv, W.; Yang, Q. H. Packing Activated Carbons into Dense Graphene Network by Capillarity for High Volumetric Performance Supercapacitors. *Advanced Science* **2019**, *6*, 1802355.
(19) Yang, X.; Cheng, C.; Wang, Y.; Qiu, L.; Li, D. Liquid-Mediated Dense Integration of Graphene Materials for Compact Capacitive Energy Storage. *Science* **2013**, *341*, 534−537.
(20) Ho, K. C.; Lin, L. Y. A review of electrode materials based on core−shell nanostructures for electrochemical supercapacitors. *J. Mater. Chem. A* **2019**, *7*, 3516−3530.
(21) Li, S.; Liang, F.; Wang, J.; Zhang, H.; Zhang, S. Preparation of mono-dispersed carbonaceous spheres via hydrothermal process. *Adv. Powder Technol.* **2017**, *28*, 2648−2657.
(22) Sevilla, M.; Fuertes, A. B. The production of carbon materials by hydrothermal carbonization of cellulose. *Carbon* **2009**, *47*, 2281−2289.
(23) Tang, K.; Fu, L.; White, R. J.; Yu, L.; Titirici, M. M.; Antonietti, M.; Maier, J. Hollow Carbon Nanospheres with Superior Rate Capability for Sodium-Based Batteries. *Adv. Energy Mater.* **2012**, *2*, 873−877.
(24) Li, Z.; Li, D.; Liu, Z.; Li, B.; Ge, C.; Fang, Y. Mesoporous carbon microspheres with high capacitive performances for supercapacitors. *Electrochim. Acta* **2015**, *158*, 237−245.
(25) Zhang, P.; Qiao, Z. A.; Dai, S. Recent advances in carbon nanospheres: synthetic routes and applications. *Chem. Commun.* **2015**, *51*, 9246−9256.
(26) Yan, Y.; Wang, T.; Li, X.; Pang, H.; Xue, H. Noble metal-based materials in high-performance supercapacitors. *Inorg. Chem. Front.* **2017**, *4*, 33−51.
(27) Zhang, L.; Candelaria, S. L.; Tian, J.; Li, Y.; Huang, Y.; Cao, G. Copper nanocrystal modified activated carbon for supercapacitors with enhanced volumetric energy and power density. *J. Power Sources* **2013**, *236*, 215−223.
(28) Ghidiu, M.; Lukatskaya, M. R.; Zhao, M.; Gogotsi, Y.; Barsoum, M. W. Conductive two-dimensional titanium carbide 'clay' with high volumetric capacitance. *Nature* **2014**, *516*, 78−81.
(29) Li, G.; Jin, R. Atomically Precise Gold Nanoclusters as New Model Catalysts. *Acc. Chem. Res.* **2013**, *46*, 1749−1758.
(30) Kaur, N.; Aditya, R. N.; Singh, A.; Kuo, T. Biomedical Applications for Gold Nanoclusters: Recent Developments and Future Perspectives. *Nanoscale Res. Lett.* **2018**, *13*, 302.
(31) Guo, H.; Qi, X.; Li, L.; Smith, R. L. Hydrolysis of cellulose over functionalized glucose-derived carbon catalyst in ionic liquid. *Bioresour. Technol.* **2012**, *116*, 355−359.

(32) Sevilla, M.; Fuertes, A. B. Chemical and Structural Properties of Carbonaceous Products Obtained by Hydrothermal Carbonization of Saccharides. *Chem. - Eur. J.* **2009**, *15*, 4195−4203.
(33) Li, M.; Li, W.; Liu, S. Hydrothermal synthesis, characterization, and KOH activation of carbon spheres from glucose. *Carbohydr. Res.* **2011**, *346*, 999−1004.
(34) Bhatia, S.; Mohr, A.; Mathur, D.; Parmar, V. S.; Haag, R.; Prasad, A. K. Biocatalytic Route to Sugar-PEG-Based Polymers for Drug Delivery Applications. *Biomacromolecules* **2011**, *12*, 3487−3498.
(35) Carabineiro, S. A. C. Supported Gold Nanoparticles as Catalysts for the Oxidation of Alcohols and Alkanes. *Front. Chem.* **2019**, *7*, 702.
(36) Rodriguez, P.; Plana, D.; Fermin, D. J.; Koper, M. T. M. New insights into the catalytic activity of gold nanoparticles for CO oxidation in electrochemical media. *J. Catal.* **2014**, *311*, 182−189.
(37) Bond, G. C.; Louis, C.; Thompson, D. T. *Catalysis by Gold*; Imperial College Press: London, 2006.
(38) Baatz, C.; Prüße, U. Preparation of gold catalysts for glucose oxidation by incipient wetness. *J. Catal.* **2007**, *249*, 34−40.
(39) Rouquerol, J.; Rouquerol, F.; Llewellyn, P.; Maurin, G.; Sing, K. *Adsorption by Powders and Porous Solids*, 2nd ed.; Academic Press: Oxford, U.K., 2014.
(40) He, Y.; Zhang, Y.; Li, X.; Lv, Z.; Wang, X.; Liu, Z.; Huang, X. Capacitive Mechanism of Oxygen Functional Groups on Carbon Surface in Supercapacitors. *Electrochim. Acta* **2018**, *282*, 618−625.
(41) Gogotsi, Y.; Simon, P. True Performance Metrics in Electrochemical Energy Storage. *Science* **2011**, *334*, 917−918.
(42) Segalini, J.; Iwama, E.; Taberna, P. L.; Gogotsi, Y.; Simon, P. Steric effects in adsorption of ions from mixed electrolytes into microporous carbon. *Electrochem. Commun.* **2012**, *15*, 63−65.
(43) Zheng, X.; Lv, W.; Tao, Y.; Shao, J.; Zhang, C.; Liu, D.; Luo, J.; Wang, D. W.; Yang, Q. H. Oriented and Interlinked Porous Carbon Nanosheets with an Extraordinary Capacitive Performance. *Chem. Mater.* **2014**, *26*, 6896−6903.
(44) Zhang, C.; Hatzell, K. B.; Boota, M.; Dyatkin, B.; Beidaghi, M.; Long, D.; Qiao, W.; Kumbur, E. C.; Gogotsi, Y. Highly porous carbon spheres for electrochemical capacitors and capacitive flowable suspension electrodes. *Carbon* **2014**, *77*, 155−164.
(45) Zhou, B.; Meng, E.; Chen, Z. Synthesis of porous carbon sphere based on starch and its application of electric double layer capacitor. *Int. J. Electrochem. Sci.* **2018**, *13*, 2441−2447.
(46) Danoglidis, P. A.; Konsta-Gdoutos, M. S.; Shah, S. P. Relationship between the carbon nanotube dispersion state, electrochemical impedance and capacitance and mechanical properties of percolative nanoreinforced opc mortars. *Carbon* **2019**, *145*, 218−228.
(47) Tang, Y.; Zhang, Y.; Rui, X.; Qi, D.; Luo, Y.; Leow, W. R.; Chen, S.; Guo, J.; Wei, J.; Li, W.; Deng, J.; Lai, Y.; Ma, B.; Chen, X. Conductive Inks Based on a Lithium Titanate Nanotube Gel for High-Rate Lithium-Ion Batteries with Customized Confi guration. *Adv. Mater.* **2016**, *28*, 1567−1576.
(48) Enustun, B. V.; Turkevich, J. Coagulation of Colloidal Gold. *J. Am. Chem. Soc.* **1963**, *85*, 3317−3328.
(49) Jagiello, J.; Olivier, J. P. Carbon slit pore model incorporating surface energetical heterogeneity and geometrical corrugation. *Adsorption* **2013**, *19*, 777−783.
(50) Banham, D. W.; Soderberg, J. N.; Birss, V. I. Pt/Carbon Catalyst Layer Microstructural Effects on Measured and Predicted Tafel Slopes for the Oxygen Reduction Reaction. *J. Phys. Chem. C* **2009**, *113*, 10103−10111.

https://dx.doi.org/10.1021/acsaem.0c01711
ACS Appl. Energy Mater. 2020, 3, 9348−9359